



Oscillation characteristics of mutually impinging dual jets in a mixing chamber

Cite as: Phys. Fluids **30**, 117102 (2018); <https://doi.org/10.1063/1.5051731>

Submitted: 11 August 2018 . Accepted: 22 October 2018 . Published Online: 13 November 2018

Mehmet N. Tomac , and James W. Gregory 



View Online



Export Citation



CrossMark

ARTICLES YOU MAY BE INTERESTED IN

[Interaction of dual sweeping impinging jets at different Reynolds numbers](#)

Physics of Fluids **30**, 105105 (2018); <https://doi.org/10.1063/1.5054161>

["Phase diagram" for viscoelastic Poiseuille flow over a wavy surface](#)


Physics of Fluids **30**, 113101 (2018); <https://doi.org/10.1063/1.5057392>



[Letter: Galilean invariance of Rortex](#)

Physics of Fluids **30**, 111701 (2018); <https://doi.org/10.1063/1.5058939>



CAPTURE WHAT'S POSSIBLE
WITH OUR NEW PUBLISHING ACADEMY RESOURCES

Learn more 



Oscillation characteristics of mutually impinging dual jets in a mixing chamber

Mehmet N. Tomac^{1,a)} and James W. Gregory^{2,b)}

¹*Department of Mechanical Engineering, Abdullah Gul University, Kayseri 38080, Turkey*

²*Department of Mechanical and Aerospace Engineering, The Ohio State University, Columbus, Ohio 43210, USA*

(Received 11 August 2018; accepted 22 October 2018; published online 13 November 2018)

In this study, we consider the oscillatory behavior of mutually impinging jets in an enclosed, dome-shaped mixing chamber. The frequency of the impinging jet oscillations is dictated by the flow rate, with the oscillatory behavior being grouped into three regimes: a low flow rate regime ($Re < 1500$), a transition regime ($1500 < Re < 2000$), and a high flow rate regime ($Re > 2000$). The detailed characteristics of the oscillations in the high flow rate regime ($Re = 6800$ in the present study) are investigated through simultaneous frequency and refractive-index-matched particle image velocimetry measurements. The oscillation mechanism in the high flow rate regime was found to be similar to that of the other two regimes, where jets collide and interact in an oscillatory manner. However, in the high flow rate regime, there is a distinct and phase-evolving process of saddle point formation and jet bifurcation that is not present at the lower flow rates. The jet bifurcation process is also distinctly related to the balance of vortical structures inside the mixing chamber, and saddle point formation plays a key role in the internal and external flow field of this configuration. The external sweep angle of the exiting jet increases with the flow rate throughout the low and transition flow rate regimes, but a constant sweep angle was found to persist in the high flow rate regime. Thus, formation and location of the internal saddle point is directly linked to the external sweep angle of the jet. © 2018 Author(s). All article content, except where otherwise noted, is licensed under a Creative Commons Attribution (CC BY) license (<http://creativecommons.org/licenses/by/4.0/>). <https://doi.org/10.1063/1.5051731>

I. INTRODUCTION

Mutual impingement of opposing jets is a widely utilized phenomenon in a variety of applications mainly due to the increased transfer and/or mixing efficiency in macro-¹ and micro-²scales. This phenomenon is recently used in the design of oscillatory devices (i.e., fluidic oscillators) to be used for other purposes such as flow control. Oscillatory behavior of impinging opposed jets is a special case among other stable flow conditions^{3,4} and is only observed if certain parameters such as the nozzle shape, the distance between nozzles, and the jet velocities are selected properly. The instabilities created by the impingement of the opposed jets at the stagnation point eventually create oscillating back pressure for the jets resulting in periodic deflection of the jets. One of the early studies pointing out this self-sustained oscillating behavior was by Nomoto *et al.*⁵ They conducted their experiments in the Re range from 20 000 to 35 000 based on the jet nozzle at various distances between two opposed nozzles and concluded that the impingement interface between the two jets is very sensitive to disturbances and that internal fluctuations of the jet itself (in the absence of external disturbances) can cause instabilities of the impingement surface which lead to self-excited oscillations. Denshchikov *et al.*^{6,7} experimentally

investigated the impingement of two identical submerged and opposed water jets at a Re of 1000. They found that a single jet always has a stable position with respect to the symmetry plane (i.e., not oscillating); however, when a second jet with mutual impingement is introduced, an initial steady stagnant region forms, followed by mutual and opposite deflection of the jets in an oscillatory manner. They reported relatively long oscillation periods, ranging from 2 to 30 s. Denshchikov *et al.* also observed that the two key parameters governing the existence or nonexistence of oscillations were the distance between jet nozzles (L) and the characteristic jet velocity (u). They discussed that the auto-oscillation behavior arises due to the unsteady pressure region formed by the collision of the jets, and after a certain amount of deflection, the jets begin to move in the opposite direction; however, they reported that the ultimate origin of the oscillations is as yet obscure. Pawlowski *et al.*⁴ numerically studied the structure and the stability of the flow field formed by impingement of two incompressible opposed jets at a nozzle-based Re below 150. They stated that the jet deflection oscillation reported by Denshchikov *et al.*⁶ starts at the Hopf bifurcation point and the symmetric steady state becomes unstable causing a stable periodic flow pattern to appear.

Li *et al.*^{8,9} studied the stagnation point offset of two opposed jets based on the distance between nozzles at different jet velocities. In the case of equal jet velocities, they reported an unstable impingement plane that oscillates between two stable positions for $2D \leq L \leq 4D$, where D is the nozzle

^{a)}Electronic mail: tomac.1@buckeyemail.osu.edu

^{b)}Author to whom correspondence should be addressed: gregory.234@osu.edu

diameter. In a later study, Li *et al.*¹⁰ stated that the self-sustained oscillations are due to the periodic pressurizing and release of pressure in the impingement region. They also investigate the effect of confinement by adding sleeves of various lengths around the jet exits and reported that confinement can prolong the oscillation period or destroy the self-sustained oscillation. Stan and Johnson¹¹ studied two opposed impinging jets up to Re of 1.1×10^4 in the turbulent regime, where Re was based on average jet velocity and jet nozzle diameter. They observed oscillations in their experiments, and the nature of these oscillations was reported to be aperiodic (no well-defined oscillations were obtained). Nevertheless, for lower Re up to 190, it was reported that the periodicity replaces itself with an unsteady behavior for higher Re , while the oscillatory behavior was observed as a result of downstream pressure fluctuations in the impingement region that propagate back to the nozzle exit.¹²

The role of impingement region pressure fluctuations on the oscillations in the case of free shear layers impinging on a solid body was also discussed based on the back pressure propagation.^{13–15} Impingement region pressure fluctuations affecting the shear layers of the jets in the vicinity of nozzles seem to be a reasonable explanation for the feedback mechanism in the subsonic regime since any downstream fluctuations will propagate back to the nozzle unless it is damped by the flow before it reaches the nozzle. Rockwell and Naudascher¹⁶ modeled the impingement area as semi-solid and reported that the deflected fluid creates a feedback loop affecting the shear layer of the jet. Also the studies of impingement of a jet on a solid surface in a confined channel report oscillations where the deflected and bifurcated jet creates perturbations on the nozzle of the jet.¹⁷ In a recent study, Hassaballa and Ziada¹⁸ concluded that this anti-symmetric flapping oscillation of the impinging jets is sustained by the high pressure in the impingement region and the feedback mechanism is mainly due to entrained region in which the small perturbations that drive the oscillations are created.

Although most of the studies in the literature consider the impingement of free jets without any nearby physical boundaries present, there are studies of mixing applications in devices such as T-jet mixers or confined impinging-jet (CIJ) mixers that consider the impingement of opposed jets in an enclosed chamber. Santos *et al.*^{19,20} investigated T-jets and CIJ mixers and discussed the existence of oscillations at the jet impingement point and the formation of coherent vortices downstream of the jets' impingement point for a particular selection of the mixing chamber width and nozzle width of the jets. Sultan *et al.*²¹ studied mixing in T-jet mixers for Re ranging from 50 to 500. They reported that oscillatory behavior is due to the dynamic evolution of the jet impingement point location that departs from the mixing chamber axis even with equal flow rates from both of the nozzles. The impingement region in these studies exhibited a chaotic flow regime where a critical Re range was observed for transition from stable laminar to unstable oscillation. Similarly Johnson^{22,23} reported a Re range of 50–100 for such transition. The existence of the oscillatory behavior in the mixing chamber that is enclosing impinging opposed jets was reported to be due to the vortices created as a result of the

unstable impingement region and pressure feedback from the walls.

Building on these prior studies, the present work delves into the details of the flow features created as a result of jet impingement in an enclosed dome-shaped chamber by investigating a special fluidic oscillator whose oscillation mechanism relies on mutual impingement of dual jets in an enclosed chamber at a relatively high Re . Fluidic oscillators are a special type of fluidic devices that produce a pulsed or sweeping jet with a wide range of frequencies when supplied by a pressurized fluid. Fluidic oscillators are usually classified into two groups. The first group is the wall attachment type of fluidic oscillator which has been studied and developed since the 1960s;²⁴ the oscillation mechanism for this type of oscillator relies on the Coandă effect and the feedback signal from the feedback channels. The second relatively new group of oscillators is referred to as the jet interaction type, which are based on the oscillation of mutually impinging jets such as the feedback-free oscillator²⁵ or the oscillator micromixer.² The geometrical configuration of the two impinging jets used in this work was inspired from the feedback-free oscillator and will be referred to as a dual jet impingement oscillator throughout this work. This oscillator creates self-sustained oscillations based on the impingement of two inclined jets and resultant vortical flow patterns in a dome-shaped mixing chamber. The dual jet impingement oscillator's geometrical outline and the schematics of the oscillatory behavior dictated by internal vortical flow patterns created by the jet impingement are shown in Fig. 1, along with the nomenclature used throughout this paper. The image on the left shows the large vortical structures created by the impingement of two jets throughout one period of the oscillator. These vortices are inherently unstable such that they cause the pair of jets to deflect in a periodic manner. Two instants of the internal flow field are shown on the right side in Fig. 1, separated by 180° phase shift. For the top right image, the upper jet is deflected toward the dome region and the lower jet is adding momentum to the exiting jet. Eventually, the lower jet is deflected toward the dome region, and this time, the upper jet is adding momentum to the exiting jet, as shown in the bottom right image of Fig. 1.

Gregory *et al.*²⁶ studied the flow field inside the mixing chamber of a dual jet impingement oscillator and reported that impingement of two jets creates an unsteady shear layer at the interface of the impingement and the shape of the shear layer changes as the jets oscillate. They also discussed that this unsteady shear layer is driven by two counter-rotating vortices (upper side and lower side vortices) and these vortices are mainly responsible for the oscillations. Gregory *et al.*²⁷ discussed that their frequency measurements indicate different flow mechanisms which might be responsible for the oscillatory behavior as the supply pressure is increased. Furthermore, they measured frequencies up to 22 kHz which were significantly higher than the oscillation frequencies measured with unconfined impinging jets. Tomac and Gregory²⁸ reported three distinct flow regimes (low flow rate, transition, and high flow rate regimes) depending on the flow rate and Re , where Re was defined based on the exit width of the oscillator and the average velocity of the exiting jet. These regimes

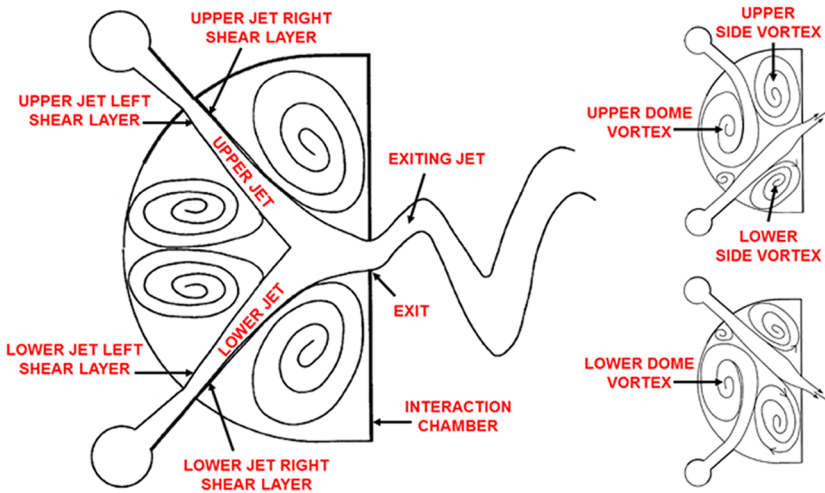


FIG. 1. Schematics of the oscillatory behavior based on diagrams by Raghu,²⁵ along with the nomenclature used in this study.

have significant similarities with some of the flow regimes discussed by Tu *et al.*²⁹ as they reported the existence of various flow regimes in the case of impingement of two jets and discussed that the flapping motion starts with impingement plane flapping, followed by a transition regime, and ending with a deflecting oscillation regime. Later Tomac and Gregory³⁰ revealed the details for the low flow rate regime for Re of 1350. They observed that the oscillation in the low flow rate regime is mainly due to the interaction of continuously impinging dual jets, interactions between dome and side vortices with limited jet bifurcation and jet deflection. In another study, Tomac and Gregory³¹ discussed the internal flow physics of the dual jet impingement oscillator in the transition regime for Re of 1680. They reported that in the transition regime each internal jet is completely deflected toward the dome region by the dome vortex once in each period. This was in contrast to the low flow rate oscillatory behavior in which the oscillations are created by continuous mutual impingement of the jets. Although these studies shed light on the flow physics of the jet impingement oscillations for the low flow rate and transition regimes, the details of the jet impingement and the oscillatory behavior were not addressed for the high flow rate regime.

In the present study, the impingement and oscillatory behavior of internal jets in a dual jet impingement oscillator are discussed mainly for the high flow rate regime at Re of 6800. The flow features were obtained with the help of simultaneous frequency and refractive index matched particle image velocimetry (PIV) measurements. The distinctive characteristics of the flow physics and oscillatory behavior in the high flow rate regime are presented with a special emphasis on the jet bifurcations as a kinetic energy transfer mechanism between impinging jets, the internal vortical balance, and the sweep angle. Results from the high flow rate regime are also compared with those from the other two regimes, providing new insights to understand the oscillation mechanisms in different flow regimes.

II. EXPERIMENTAL SETUP

A refractive index matched PIV technique along with a custom microphone-tube sensor configuration and a

quarter-period based phase-averaging method were used to extract the internal flow field of the oscillator (see Ref. 30 for details). The general geometrical outline of the tested dual jet impingement oscillator model is shown in Fig. 2. This experimental model was built from clear acrylic by laser cutting, with the dome-shaped mixing chamber measuring 12.5 mm wide \times 15 mm long \times 1.5 mm deep, with an internal nozzle width (E) of 1.70 mm and an exit nozzle width (B) of 2 mm. The angle between the internal jets and the mixing chamber center line is 58° , for a total angle between impinging jets of 116° . Other important dimensions such as the distance from the internal jet exit midpoint to the mixing chamber center line are also provided in Fig. 2.

The clear acrylic material that was used to manufacture the experimental model has a refractive index of 1.49 at a wavelength of 589 nm, while air has a refractive index of 1.00 and water has a refractive index of 1.33 at the same wavelength. When air or water is used as the supply fluid, unpreventable reflections due to the laser illumination diminish the quality of the experimental data significantly. Furthermore, substantial information about the flow field might be lost particularly in small-scale models because of these reflections. The model used in this study is a small scale model; thus, unaddressed reflections were expected to affect the entire measured flow field of the oscillator. To prevent these reflections, a refractive index matched solution was prepared, consisting of 60% NaI by weight, with 5.50 kg of NaI added to 3.66 kg of

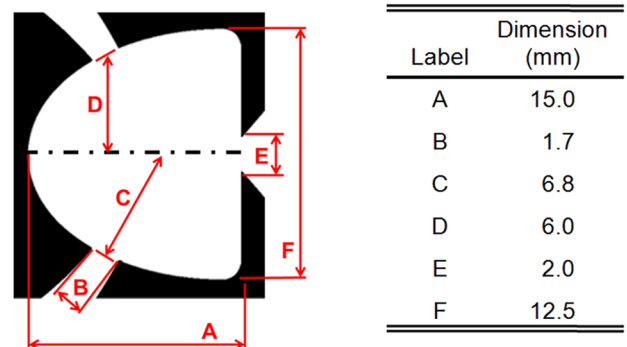


FIG. 2. Geometric dimensions of the experimental model.

distilled water to yield 5 l of NaI solution with a density of 1730 kg/m^3 . This solution has a refractive index around 1.50, which is very close to that of acrylic. Hollow glass spheres (HGS) from Lavision, Inc., with a density of 1200 kg/m^3 and mean particle size of $10 \text{ }\mu\text{m}$ were added as tracer particles to the NaI solution. Although denser tracer particles such as silver-coated HGS (density 1650 kg/m^3) are almost a perfect match for NaI solution, the chemical properties of iodide inhibited the use of silver-coated spheres since iodide reacts with silver. Unfortunately, the difference in density was inevitable for this experimental setup, but it was determined that buoyancy-induced velocity errors were negligible ($\pm 10^{-4} \text{ m/s}$).

The orientation of the experimental model and a schematic of the experimental setup used for the refractive index matched PIV measurements are presented in Fig. 3. The PIV system consisted of a 15 Hz 200 mJ double-pulsed Nd:YAG 532 nm laser (New Wave Solo XT 200) with sheet-forming optics (spherical and cylindrical lenses), a programmable timing unit (LaVision External PTU V. 9.0), and a charge-coupled device (CCD) camera (PCO 1600) with a macro-lens (Sigma 105 mm, 1:2.8D). The time separation between two laser illuminations was $100 \text{ }\mu\text{s}$, and LaVision's Davis software was used for data acquisition and post-processing, in conjunction with LabView 8.6 and MATLAB R2011b. The image pairs were acquired at a rate of 3.75 Hz, yielding 160 s of total recording time. Six hundred image pairs were acquired in the high flow rate regime simultaneously with the frequency measurement, and one period of the oscillation was divided into 40 phases. Each bin covers a phase angle range of 9° , and the images that fell into the same bin were averaged. The maximum number of images in each phase bin was 19, and the minimum number of images was 11. In Davis, each image pair was cross-correlated with multi-pass processing (64×64 and 32×32 window size) with 50% overlap with the neighboring window and post-processed with the help of a median filter to remove spurious vectors. Furthermore, a 3×3 Gaussian smoothing filter was applied to the velocity vector fields. For the Re considered in this study and the PIV system used, the uncertainty in the u and v (velocities along the x and y axes, respectively, as shown in Fig. 3) components of the velocity was estimated to be ± 0.1 and $\pm 0.12 \text{ m/s}$,

respectively. The oscillation frequency for the flow rate presented in this work was 78.9 Hz, with an average period of 12.67 ms.

A flow meter (Omega Engineering FLR1011ST) was used along with a precision needle valve to control the flow rate. The flow meter was calibrated before the experimental trials with the help of a container, a stopwatch, and a graduated cylinder. For the flow rate considered, the uncertainty in the flow rate measurements was estimated to be $\pm 3\%$ of the measured flow rate. The temperature of the NaI solution was measured with a K-type thermocouple (NI USB-TC01) and calibrated with a thermometer having $0.1 \text{ }^\circ\text{C}$ divisions (Kessler Thermometer Corp. 2100-3). Temperature measurements allowed instant calculation of the density and the viscosity of the NaI solution during the experiments. Since the use of a hot film probe was impossible due to the electrochemical properties of the NaI solution, a condenser microphone (Radioshack 270-0092) sensor configuration was used for frequency measurements. As seen in Fig. 3, while the condenser microphone was placed in a Tygon tube with 8 mm ID keeping the microphone away from the NaI solution, a bent metal tube with 1 mm OD was located in the vicinity of the oscillator exit. Repeated measurements ($N = 100$) resulted in an uncertainty of $\pm 4\%$ of the measured frequency. Further details about this experimental setup, the custom microphone-tube sensor configuration, and the quarter-period based technique used to avoid jitters in the PIV phase-averaging process are provided by Tomac and Gregory.³⁰

III. FREQUENCY CHARACTERISTICS

Tomac and Gregory²⁸ reported the existence of the three flow rate regimes when the frequency characteristics of the oscillator are considered. Boundaries of these flow regimes for the experimental model used in this study are provided in Fig. 4 for flow rates from 2.8 ml/s to 15 ml/s, corresponding to a Re range from 1350 to 7300 (based on the exit width of the oscillator and the average velocity of the exiting jet). The variation of frequency with flow rate is linear but discontinuous in the transition regime with a reduction in slope after this narrow transition region. The transition regime marks a change in the fundamental nature of the oscillations, as documented by Tomac and Gregory.³¹ The focus of the present paper is on the jet impingement and the oscillatory behavior of the oscillator in the high flow rate regime at a volume flow rate of 14 ml/s ($Re = 6800$), as shown with the black arrow in Fig. 4(a). The distinctions between the flow rate regimes are clearer when the Strouhal number (St),

$$St = f \times D/u, \quad (1)$$

is used, where f is the measured frequency of the exiting jet in Hz, D is the distance from the internal jet exit midpoint to the mixing chamber center line (see Fig. 2), and u is the mean velocity of an internal jet calculated from the measured flow rate. The non-dimensional representation of the data is in Fig. 4(b), where the Strouhal number range was between 0.11 and 0.19 for this Re range. A similar Strouhal number range (based on the impingement distance between nozzles and the centerline velocity of the exit nozzle) of 0.1–0.16 was

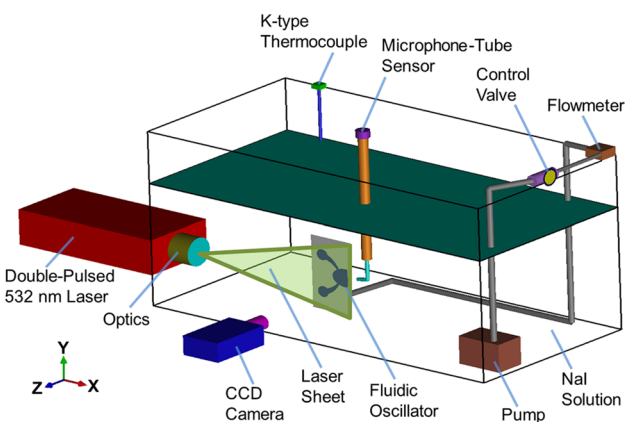


FIG. 3. Schematic of the refractive index-matched PIV setup.

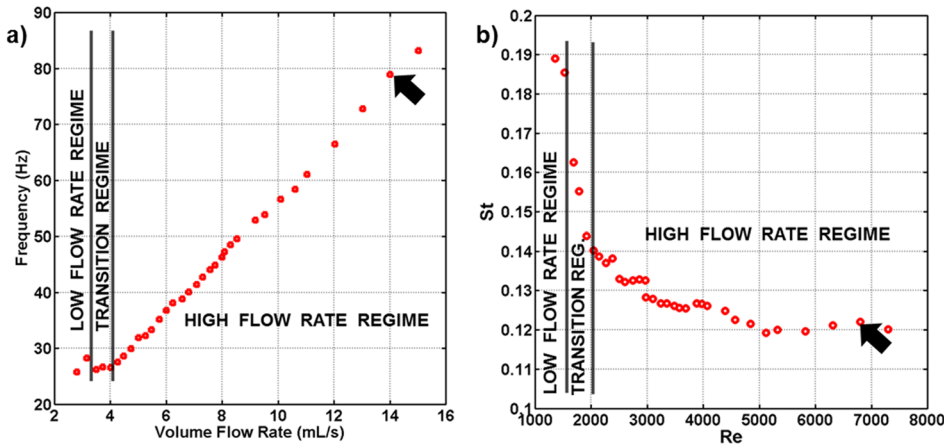


FIG. 4. Flow rate-frequency characteristics of the oscillator, in (a) dimensional and (b) nondimensional forms. Figure (a) reprinted with permission from M. N. Tomac and J. W. Gregory, “Internal jet interaction in a fluidic oscillator at low flow rate,” *Exp. Fluids* **55**(5), 1730 (2014). Copyright 2014 Springer Nature.

reported by Hassaballa and Ziada¹⁸ for the Re range from 2×10^4 to 3.3×10^4 , while Li *et al.*¹ reported Strouhal numbers (based on the nozzle separation distance and the exit bulk velocity) between 0.1 and 0.2 for the Re range from 786 to 6288 (where Re was based on the nozzle height and the exit bulk velocity of the jets for both studies). The significant drop in frequency at about $Re = 1500$ corresponds to the transition regime; the black arrow in Fig. 4(b) shows the selected Re for this study (6800), where the oscillation frequency was 78.9 Hz.

IV. DUAL JET IMPINGEMENT AND THE OSCILLATORY BEHAVIOR IN THE HIGH FLOW RATE REGIME

A. Flow features and the oscillation mechanism

Oscillations created by dual jet impingement in a mixing chamber are due to interaction of many interesting flow features. While these oscillatory characteristics were discussed in other studies for the low flow rate³⁰ and the transition³¹ regimes, the details of the flow in the high flow rate regime are substantially different and are the main subject of the current work. Figures 5–11 document the internal velocity magnitude and vorticity fields, with superimposed streamlines, at several phase positions throughout a cycle of the oscillations. These figures serve as the basis for the following overview of the oscillatory mechanisms. The key mechanism of the oscillation in the high flow rate regime relies on the motion and

bifurcation of the jets, the interaction between three main vortices, and the mutual interaction between the jets and vortices. Two side vortices formed inside the mixing chamber on either side of the oscillator exit are persistent and never vanish; however, they do change shape, strength, and orientation throughout the oscillation period. On the other hand, the vortex that appears and vanishes in the dome region is created once by each jet in each period (two separate instances of the dome vortex, of opposite sense). As this dome vortex grows, it entertains some portion of the opposed jet by means of jet bifurcation. This can be observed through the existence of a saddle point indicating that the bifurcation process is taking place. By this bifurcation mechanism, some of the momentum of the opposed jet is transferred to the other jet. As the bifurcation continues, the opposed jet is deflected increasingly toward the dome region until it is fully deflected and is no longer supplying momentum to the exiting jet directly. At this point, the dome vortex and the saddle point vanish, and a new dome vortex is created and supplied by the fully deflected jet. The same pattern repeats itself, and this constitutes the auto-oscillation mechanism of the dual jet impingement oscillator.

The distinct flow physics of the oscillatory behavior in the high flow rate regime can further be described in detail by using the nomenclature that was introduced in Fig. 1. At a phase angle of 0° (Fig. 5), the upper jet is the dominant jet, where it is the primary source of momentum for the exiting jet. Here, the lower jet is moving toward the exit due to the

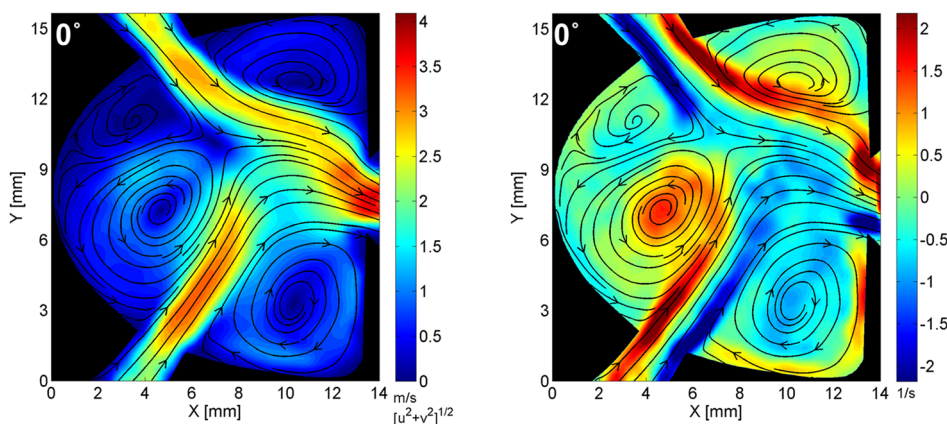


FIG. 5. Streamlines superimposed on velocity (left) and vorticity (right) contours at 0° phase angle.

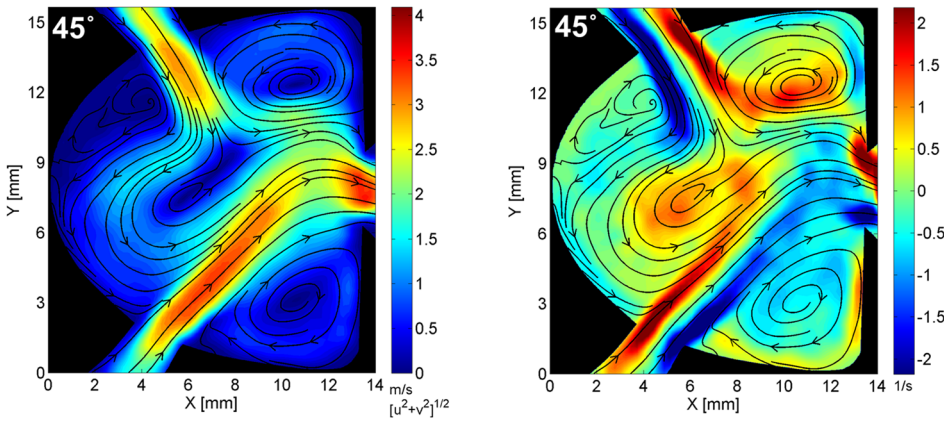


FIG. 6. Streamlines superimposed on velocity (left) and vorticity (right) contours at 45° phase angle.

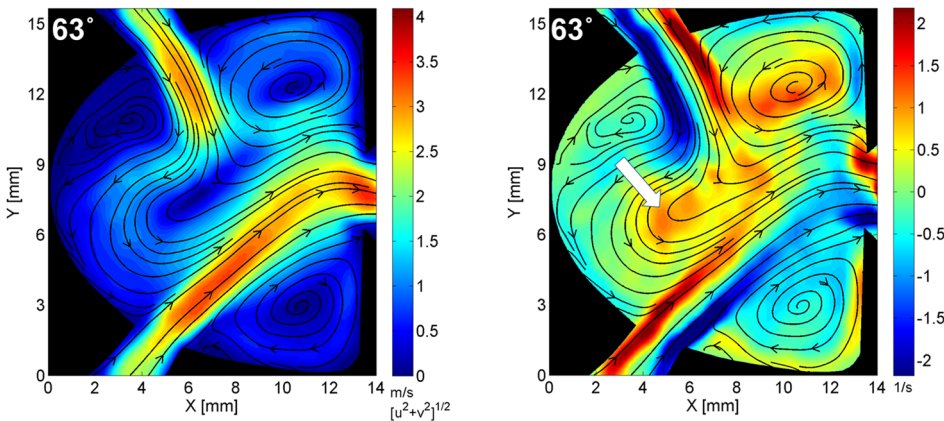


FIG. 7. Streamlines superimposed on velocity (left) and vorticity (right) contours at 63° phase angle.

increasing size and strength of the lower dome vortex, and as a consequence, the lower jet bends the upper jet. The dome vortex created by the lower jet has reached the upper jet and created a saddle point, indicating that the upper jet is being bifurcated into two parts. The left branch of the bifurcated upper jet flows over the dome vortex as this vortex rolls up, and the right branch of the upper jet is still connected with the exiting jet and does not add momentum to the upper side vortex. The lower jet right shear layer extends up to the upper jet right shear layer. Note that the interaction of either jet (lower or upper jet) with the corresponding side vortex (lower side or upper side vortex) is continuous, but the strength of this interaction changes throughout the oscillation period.

At a phase angle of 45° (Fig. 6), the saddle point has moved further toward the exit centerline and is about to vanish. A large portion of the bifurcated upper jet coalesces with the lower jet through the dome-shaped region and leaves the oscillator, while both the lower jet and the upper jet bifurcated branches are adding momentum to the upper side vortex. However, the lower jet does not add any momentum to the lower side vortex. The vorticity contours indicate that the lower jet left shear layer is about to stop adding momentum to this vortex, which will cause decay of the lower dome vortex.

The results for the phase angle of 63° are presented in Fig. 7. For this phase angle, the saddle point vanished as the dome vortex decays, and as a result, the upper jet is not adding

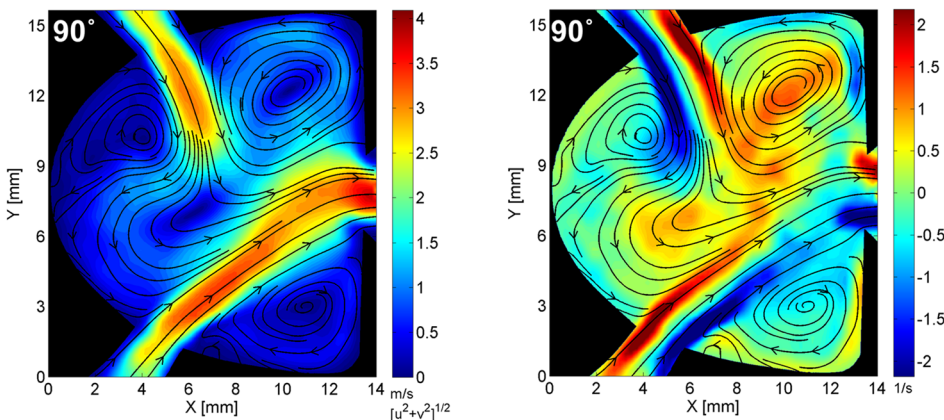


FIG. 8. Streamlines superimposed on velocity (left) and vorticity (right) contours at 90° phase angle.

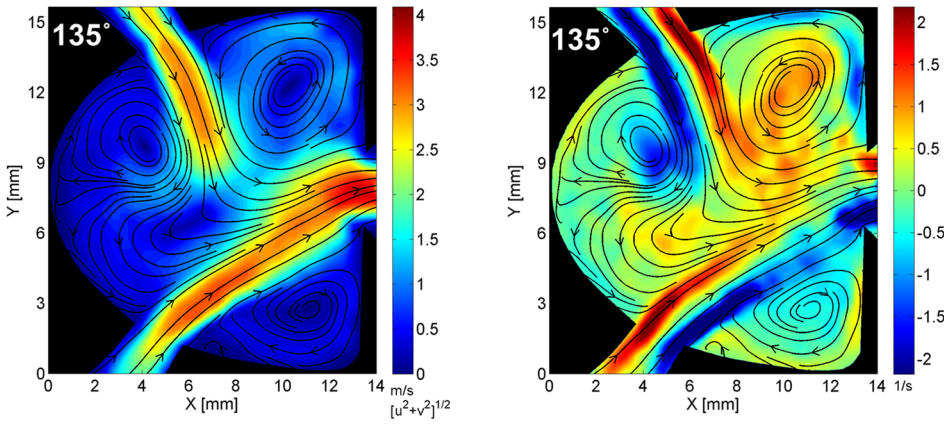


FIG. 9. Streamlines superimposed on velocity (left) and vorticity (right) contours at 135° phase angle.

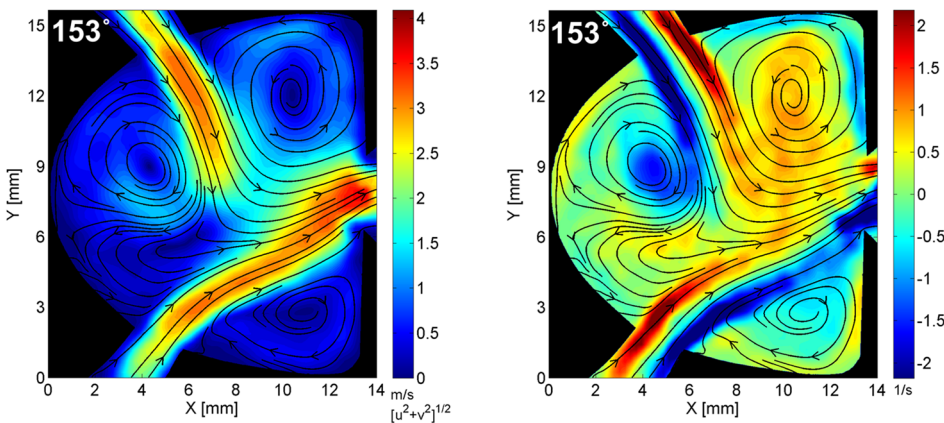


FIG. 10. Streamlines superimposed on velocity (left) and vorticity (right) contours at 153° phase angle.

momentum to the exiting jet. The lower jet is adding momentum to the exiting jet at this instant. The newly growing upper dome vortex constricts the left branch of the upper jet, while the right branch of the upper jet is adding momentum to the upper side vortex causing an increase in the secondary vorticity in the boundary layer above the wall. The lower jet left shear layer is no longer adding momentum to the lower dome vortex; however, a region of strong vorticity in the dome-shaped region is a remnant of the lower dome vortex from previous phases and is shown with the white arrow in the vorticity contours.

At a phase angle of 90° , the upper dome and upper side vortices are growing in size, while the lower side vortex loses its strength, as shown in Fig. 8. At this instant, the upper side

vortex is keeping the upper dome vortex deflected in the dome-shaped region since both the upper jet right and lower jet left shear layers are adding momentum to the upper side vortex. On the other hand, the strong vorticity region that was previously pointed out by the white arrow in Fig. 7 is still present but at a diminished strength. Furthermore, the potential core of the lower jet is entirely connected with the exiting jet.

Figure 9 shows the results for a phase angle of 135° . At this instant, the upper dome vortex, fed by the upper jet left shear layer, gets stronger and larger and pushes the upper jet toward the exit. At the same time, the upper dome vortex entrains the left branch of the upper jet, thus decreasing the portion of the bifurcated upper jet that coalesces with the lower jet.

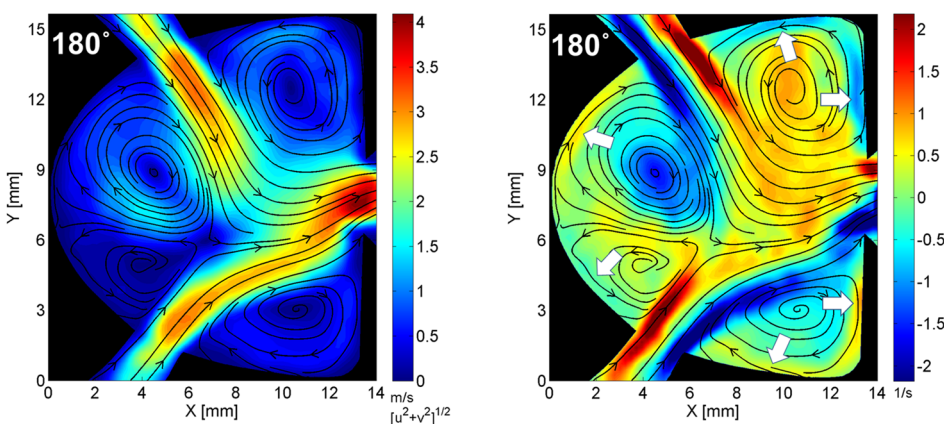


FIG. 11. Streamlines superimposed on velocity (left) and vorticity (right) contours at 180° phase angle.

Both the upper and lower jet right shear layers are adding momentum to the upper side vortex. The remnant vorticity from the decay of the lower dome vortex is being entrained by the upper dome vortex. Similarly, for the phase angle of 153° shown in Fig. 10, the upper dome vortex is larger in size and strength and increasingly deflecting the lower jet, while almost all the left bifurcated branch of the upper jet is entrained by the upper dome vortex. As the upper jet is pushed toward the exit in consecutive phases, it bends the lower jet more and causes the lower jet to change the flow direction of the exiting jet in a continuous manner. This effect can be observed by following the direction of the streamlines at the exit of the oscillator in Figs. 7–10.

At a phase angle of 180° (Fig. 11), the flow field is the mirror image of the data from zero phase angle (Fig. 5). At this instant, a large upper dome vortex starts formation of the

saddle point, indicating that the bifurcation process has started for the upcoming half cycle. Also, the direction of the flow in the dome-shaped region is from the lower jet to the upper jet, in contrast with the first half cycle of the oscillation described so far. The lower jet is deflected by the upper jet, while the deflected lower jet has trapped the lower side vortex; the potential core of the lower jet is still adding momentum to the exiting jet. The upper side vortex region exhibits higher levels of vorticity strength than the previous flow rate regimes. Note that the white arrows in the vorticity contour plot in Fig. 11 point to the wall boundary layers which contain increased vorticity; this arises from the wall-normal velocity gradient set up by the nearest vortex structure.

A phase angle of 180° indicates that half of the oscillation cycle is completed. After this point, the underlying oscillation mechanism repeats itself in turn for the other jet to be

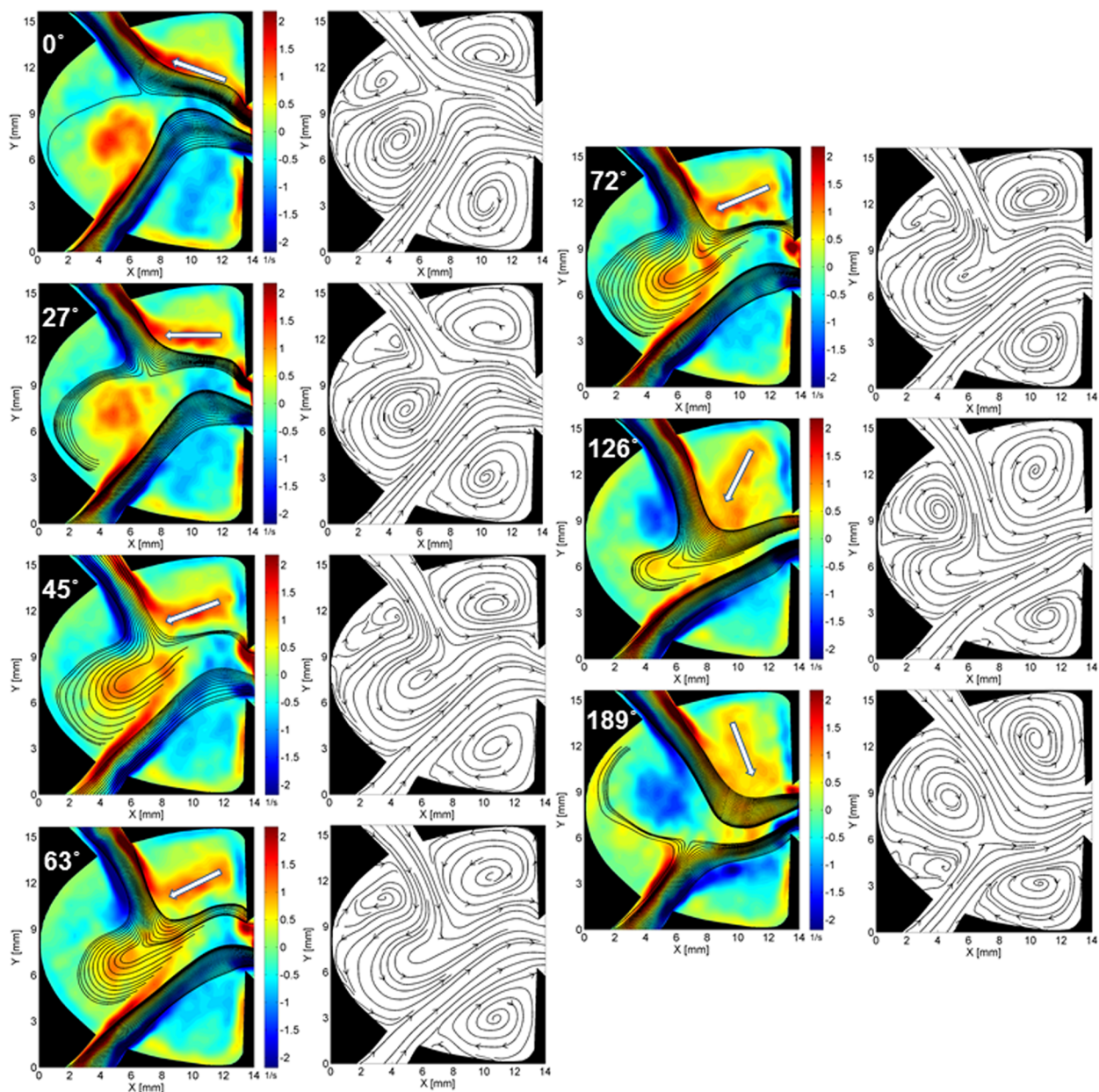


FIG. 12. Dense inlet streamlines superimposed on vorticity contours (color images with the color bars) and streamlines (black and white images without color bars) at a phase angle range of 0° – 189° at Re of 6800.

deflected. The critical phenomena driving the oscillations—including jet interactions, bifurcations, deflection, and the vortical balance—can be summarized as follows. A side vortex pushes an adjacent jet (e.g., the upper side vortex pushes the upper jet), which in turn initiates the creation of the dome vortex. As this dome vortex grows, it pushes the adjacent jet toward the exit while also deflecting the opposing jet at a different location for each consequent oscillation phase, thus causing the exiting jet to continuously change the flow direction. However, when the adjacent jet reaches the opposing jet, it starts bifurcating the opposite jet. This bifurcation process manages the transfer of the momentum of a jet to the opposing jet—thus, there is a perpetual imbalance in the momentum of the two jets and continuous mixing of the two jets.

B. Jet bifurcations

Jet bifurcations were observed to play a vital role in the momentum transfer between the jets and are explored in further detail. Figure 12 shows plots of the vorticity contours overlaid with a set of dense inlet streamlines, and next to each figure are the streamlines inside the oscillator for each phase. For the phase angle of 0° , the lower dome vortex has just reached the upper jet and started bifurcating it. At the phase angle of 27° , a larger portion of the upper jet is bifurcated as the dome vortex moves further toward it. On the other hand, at a phase angle of 45° , only a small portion of the upper jet remains without being bifurcated by the lower dome vortex. This small portion consists of constricted streamlines between the upper side vortex and the lower jet. For the phase angle of 63° , the saddle point appears to have vanished. Interestingly, the saddle point re-appears at a phase angle of 72° , causing a temporary increase in the amount of the bifurcated portion of the upper jet. At the phase angle of 126° , the bifurcated portion of the upper jet is more constricted by the upper dome vortex, and at a phase angle of 189° , the upper dome vortex is bifurcating the lower jet this time as the saddle point indicates this process. Furthermore, in this figure, the white arrow tracks the changes in the orientation of the high vorticity region at the upper side vortex throughout the presented phases, showing how the upper jet's right shear layer acts in the side region. When these arrows are considered along with

the streamlines in the white and black images in Fig. 12, it can be seen that the changes in the shape of the side vortices are dictated by the orientation of this high vorticity region and these changes are the result of the interaction between the shear layers of the jets and the vortical balance inside the oscillator.

Detailed observations of the inlet streamlines and the saddle point formations suggest that once the dome vortex-saddle point pair forms, this topology is sustained until the bifurcated jet's momentum addition to the exiting jet is completely terminated. In fact, the presence of the dome vortex-saddle point pair is sustained for approximately one-third of the period. Figure 13 presents an analysis of the portion of the bifurcated jet that exists in the dome region throughout the oscillation period. These results for the bifurcated portion were obtained by simply dividing the number of bifurcated inlet streamlines by the total number of inlet streamlines. As seen in this figure, each jet remains bifurcated for about 37.5% of the oscillation period (total of 75% for both jets) and for 12.5% of the oscillation period a saddle point is observable (total of 25% for both jets) in the data presented in Fig. 12. Points *A* and *D* show the maximum bifurcated portion for the upper and the lower jets, respectively. These peaks correspond to the phase positions where the saddle points vanish; however, as mentioned earlier, both jets remain bifurcated for a while due to the energy stored in remnant vorticity from the decayed dome vortex (i.e., while no further vorticity is being added to the dome vortex, the dissipation of vorticity left from the decayed vortex takes time and continues to affect jet bifurcation). Interestingly, from points *B* to *C* and points *E* to *F*, the percent of the bifurcated portion of the jets increases. At these very points, it was found that the saddle points momentarily re-appear but completely vanish immediately thereafter. The reason for this might be the change in the deflected jet in the dome region. For instance, for point *B*, the upper jet is still deflected, but for point *C*, the lower jet is being deflected and replaces the upper jet in the dome region. Points *B* and *C* correspond to phase angles of 63° and 72° , respectively, and the increase in the bifurcated portion can be seen in Fig. 12. On the other hand, as the upper dome vortex grows, it constricts the bifurcated portion of the jet between itself and the other jet and eventually the percent of the bifurcated portion of the jet starts decreasing after point *C* or *F*.

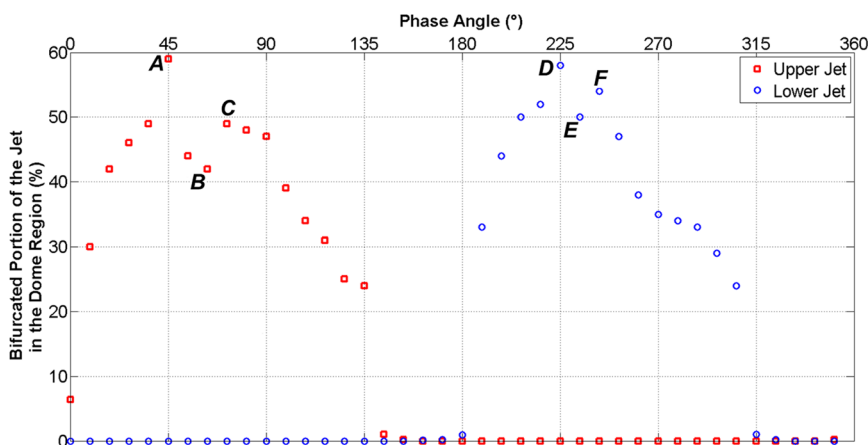


FIG. 13. Bifurcated portion of a jet in the dome region (%).

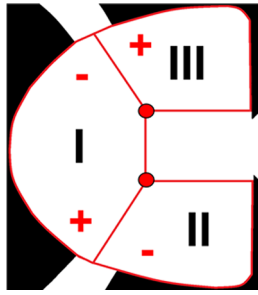


FIG. 14. Boundaries of average vorticity calculation regions and vorticity sign of each vortex.

C. Vortical balance

The jet bifurcation process was observed to be an essential component for momentum transfer between the upper and lower jets in the high flow rate regime. Another important phenomenon is the vortical balance inside the mixing chamber. In order to obtain the details of the internal vortical balance, the following approach was adopted. The oscillator's mixing chamber was divided into three regions based on the separate locations of the characteristic vortices (i.e., dome vortices and side vortices) as seen in Fig. 14 along with the vorticity signs. In this figure, region I encompasses both the lower dome vortex with counter clockwise (+) vorticity and the upper dome vortex with clockwise (−) vorticity, which are present at different phases of the oscillation. Region II encompasses the lower side vortex with clockwise (−) vorticity, and region III encompasses the upper side vortex with counter-clockwise (+) vorticity. The unnamed volume between regions II and III was ignored since it does not encompass any significant vorticity. Once the boundaries of these three regions were defined,

the average vorticity in each region was calculated for each phase.

Figure 15 shows the average vorticity data for all three regions for two periods of the oscillation. The results such as the peak values for the lower dome vortex and the upper dome vortex should be identical in ideal conditions; however, they differ by a maximum vorticity of 0.12 s^{-1} . This may be due to the buoyancy effects on the seed particles in the low-velocity vortical regions. Nevertheless, no other measurement of the internal flow exhibits asymmetry, and the results in Fig. 15 provide many interesting insights into the oscillations mainly at the points (A to J) shown. Furthermore, in this figure, the absolute value of average vorticities was provided to ease the comparison between different regions.

Point A in Fig. 15 corresponds to a point in which the magnitude of the average vorticity in regions II and III is equal at 0.33 s^{-1} , and these vortices balance each other. Interestingly, the average vorticity in the dome vortex region marked with *point B* is very close to zero for the same phase angle. Likewise for *points F* and *G*, a similar relationship also holds. Therefore, since the dome vortex region has zero average vorticity and the side vortices' average vorticities are equal, the oscillator can be considered as “vortically balanced” for this phase. In order to observe the changes in the internal flow field of the oscillator around *points B* and *G* (zero vorticity for the dome vortex region), vorticity contours with the superimposed streamlines are evaluated, as shown in Fig. 16. Results indicate that *points B* and *G* are the points at which the saddle points (shown with black arrows) vanish and the dome vortices are no longer fed by the shear layers of the jets. For instance, at the phase before *point G* (225°), a saddle point exists while the phase after *point G* (234°) indicates that

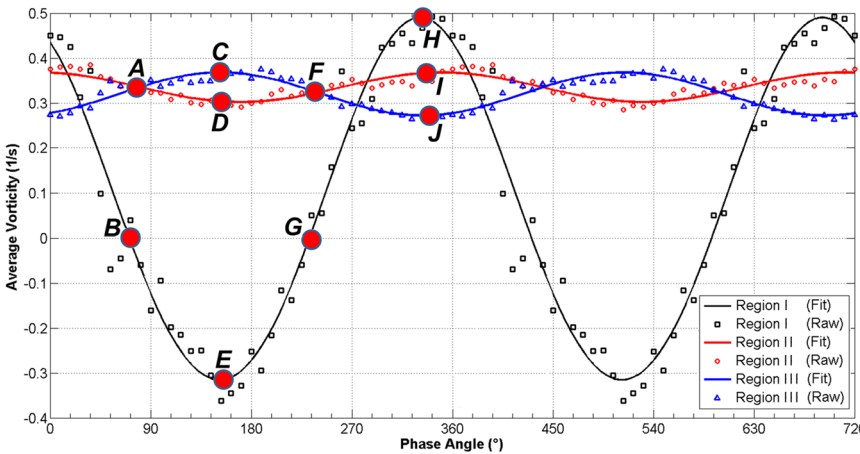


FIG. 15. Internal average vorticity balance for the side and dome vortices in the three vortex encompassing regions.

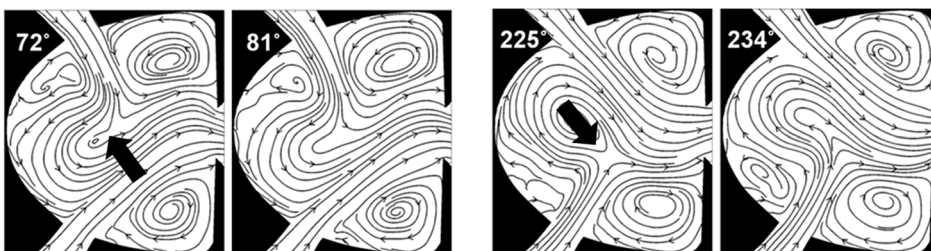


FIG. 16. Change in the internal flow field before (72° and 225°) and after (81° and 234°) *point B* (left two images) and *point G* (right two images).

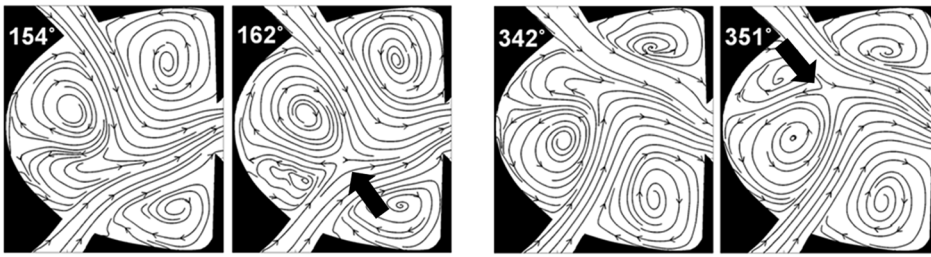


FIG. 17. Change in the internal flow field before (154° and 342°) and after (162° and 351°) points C-D-E (left two images) and points H-I-J (right two images).

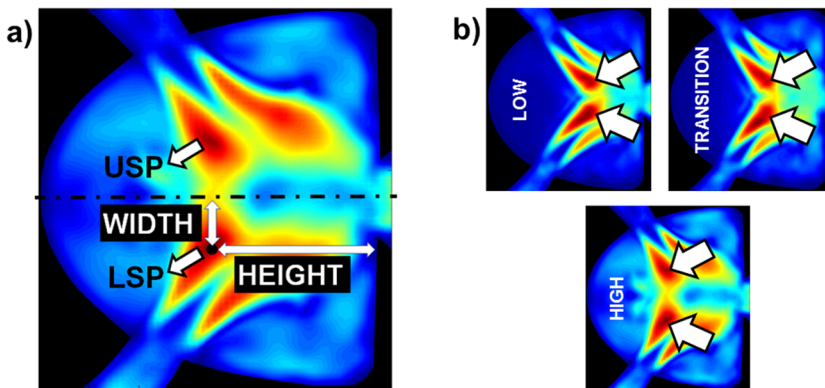


FIG. 18. Definition of the saddle point height and width, the location of the upper and lower saddle points (a), and saddle point characteristics in the three flow rate regimes (b).

the saddle point has vanished. These results interestingly confirm the complete vanishing of the saddle points as was shown as *points C* and *F* in Fig. 13. Vanishing of a saddle point is important since it also indicates the decay of a dome vortex. Therefore, the average vorticity in region I first approaches to zero and switches sign when the saddle point vanishes, indicating another new dome vortex is being created by the opposite jet.

Two other sets of points that yield interesting results are *points C-D-E* and *points H-I-J*. Figure 17 shows the streamlines superimposed on vorticity contours for phase angles of 154° and 162° which are before and after *points C-D-E* and for phase angles of 342° and 351° which are before and after *points H-I-J*. Between phase angles of 342° and 351°, the lower dome vortex dominates the dome vortex region and bifurcates the upper jet (evidenced by the saddle point, identified by the black arrow in Fig. 17). Interestingly, when the lower dome vortex causes a positive vorticity peak at *point H*, the lower side vortex region’s average vorticity hits its peak at *point I* and the upper side vortex hits its lowest average vorticity magnitude at *point J*. After the lower dome vortex hits its average vorticity peak, it loses its strength due to entrainment of the upper jet in the bifurcation process. A similar process also takes place for *points C-D-E*. Therefore, these points show the phase in which a saddle point is created by a dome vortex and the bifurcation process is started.

V. CHANGE OF CHARACTERISTICS WITH THE FLOW RATE

It was observed that the oscillatory behavior in the high flow rate regime is similar to that of the low flow rate and the transition regimes. However, the location of the saddle point

was observed to differ between these flow rate regimes. In order to quantify this difference, period-averaged RMS velocity magnitude fluctuations were calculated. This calculation provides images as shown in Fig. 18. In this figure, the locations of the saddle points were determined based on the fact that saddle points are associated with the high velocity fluctuations;³² thus, the points of highest RMS fluctuations are indicators of the saddle point locations (also referred to as stagnation points in the bifurcation analysis study of Pawlowski *et al.*⁴). The saddle point created by the upper jet is called the upper saddle point (USP), and the saddle point created by the lower jet is called the lower saddle point (LSP), while the

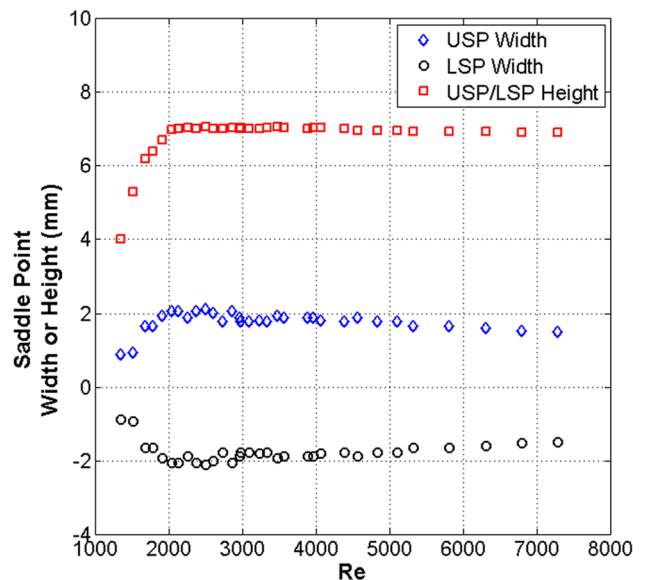


FIG. 19. Saddle point width and height change with *Re*.

definition of the saddle point height and width is also shown in Fig. 18(a). In Fig. 18(b), the locations of the saddle points were shown for all three flow regimes. As can be seen in the figure, the saddle point moves closer to the dome region as the flow rate is increased. Note that color bars for these three images are different, but most fluctuating regions were visible as dark red contours in each of the image.

Figure 19 shows the USP and the LSP widths and height depending on the flow rate. Similar to the findings of Pawlowski *et al.*,⁴ the results suggest that the pitchfork bifurcation is responsible for transitioning the oscillator from a single steady state to multiple steady states as the flow rate is increased. In the low flow rate and transition regimes ($Re < 2000$), the saddle point height and width increase with increased flow rate until $Re = 2000$. Beyond this critical

Reynolds number and into the high flow rate regime, the saddle point height remains relatively stable and the saddle point width decreases slightly.

The location of the saddle point was observed to directly and significantly affect the sweep angle of the exiting jet. In contrast to the low flow rate and the transition regimes, the sweep angle does not change significantly in the high flow rate regime and this is mainly due to the fact that the location of the saddle point dictates the deflection of a jet and the deflected jet dictates the sweep angle. Flow visualizations were used in order to quantify the changes in the sweep angle of the oscillator with increasing flow rate. Figure 20 shows the flow visualization images for the Re range of 800–7000. As seen in visualizations, for Re below 2000, the sweep angle is increasing; however, after this Re , the sweep angle is constant

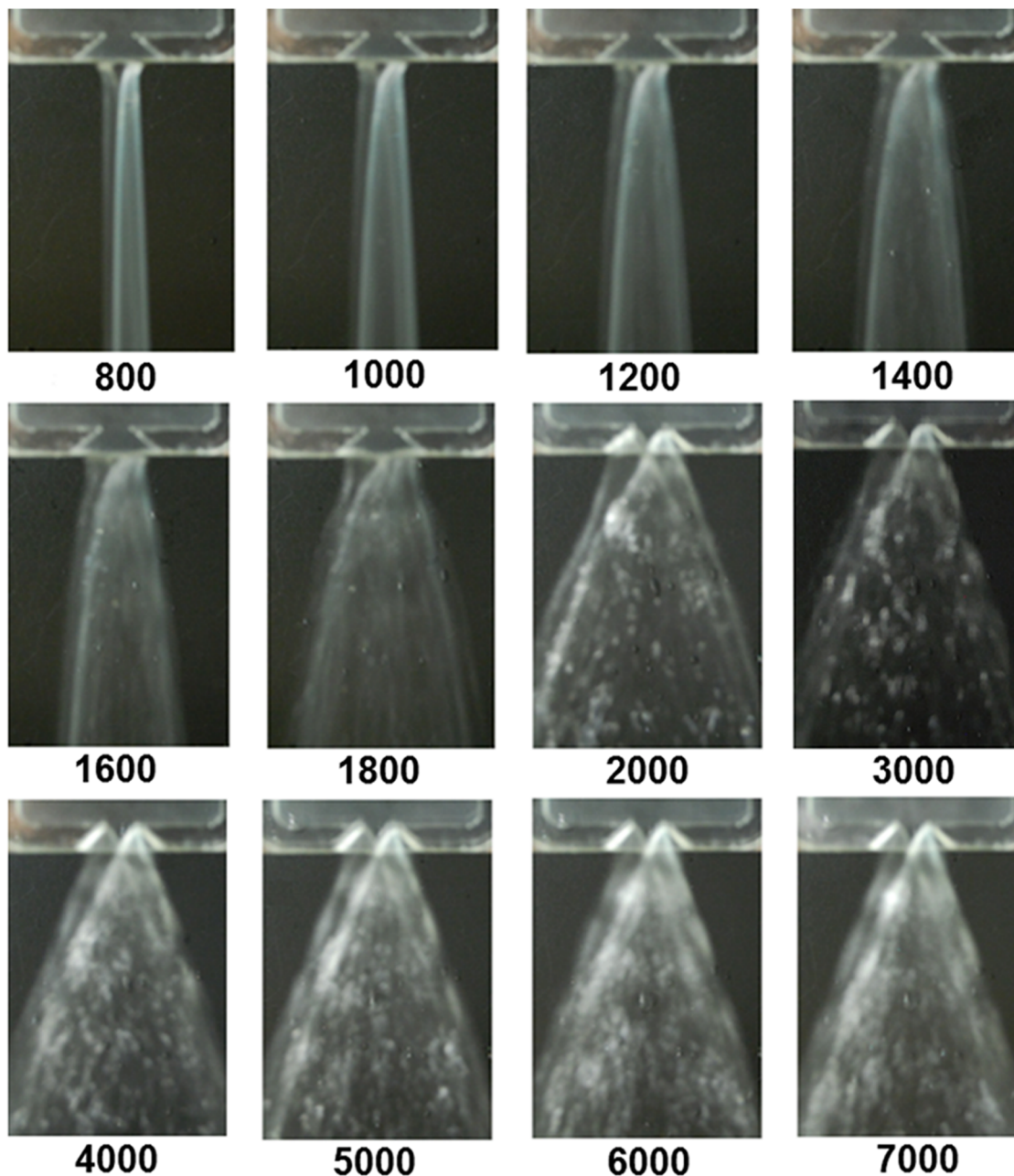


FIG. 20. Flow visualizations of the sweep angle increasing with Re .

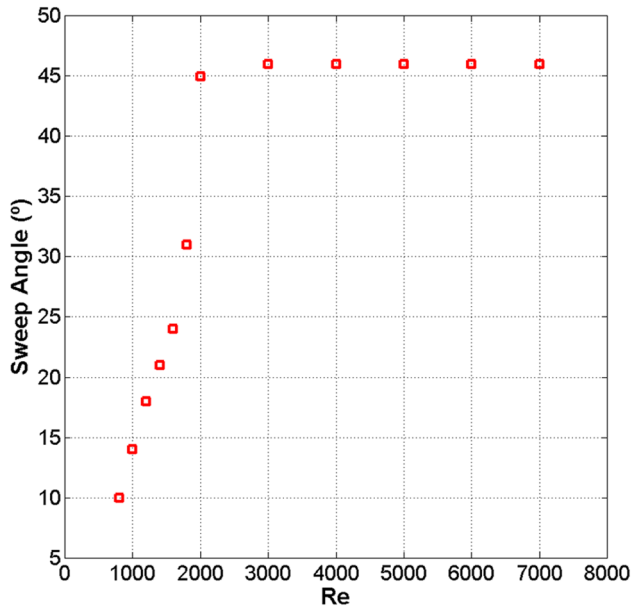


FIG. 21. Change in the sweep angle with the Re .

around 46° . Furthermore, while the flow is smooth up to Re of 1600, a higher level of unsteadiness is evident for Re higher than 1600. The sweep angles were measured directly from these flow visualization images and are presented in Fig. 21. In the low flow rate and transition regimes, the sweep angle continues to increase until the high flow rate regime begins. After this regime begins, the heights of the saddle points are stable and the sweep angle does not change with a further increase in the flow rate.

VI. CONCLUSION

Refractive index matched PIV and frequency measurements were used to investigate the dual jet impingement and oscillatory behavior of an oscillator in the high flow rate regime at Re of 6800. Internal jet mixing characteristics for the high flow rate regime are distinctly different from the low flow rate and transition regimes: whereas the jets continuously collide in the low flow rate and transition regimes, in the high flow rate regime, a saddle point forms and the jets bifurcate. In this high flow rate regime, a dome vortex created once per period by each jet is responsible for the bifurcation and complete deflection of the opposing jet. The dome vortex also forms a saddle point that eventually reaches the opposite jet and changes the direction of flow in the dome region when it starts deflecting the opposed jet. Saddle point formation is the key indicator of the jet bifurcation process, which also governs the momentum transfer between the jets. Each jet was observed to be bifurcated for about 37.5% of the oscillation period (total of 75% for both jets), whereas the saddle point for each jet was observable for 12.5% of the oscillation period. Therefore, the excellent mixing characteristics of the dual jet impingement oscillator are due to the fact that at least one of the jets is bifurcated for most of the period and because the bifurcated jet coalesces with the opposing jet.

The internal mixing chamber was segmented into three parts for assessment of vortical balance throughout the

cycle—one region encompasses the dome vortex, while the other two regions account for the side vortices. Whenever the average vorticity of the side vortices is equal, the average vorticity in the dome vortex region is zero, the dome vortex at that particular phase angle is evanescent, and the saddle point vanishes. The saddle point reappears when the average vorticity in the dome vortex region reaches a maximum and the vorticity for each side vortex reaches an extremum.

Furthermore, saddle point formation locations were found to be the main parameter dictating the sweep angle of the oscillator for a given flow regime. These saddle point formation locations were observed to be stable in the high flow rate regime resulting in a constant sweep angle throughout this regime, in contrast with an increasing sweep angle in the low flow rate and the transition regimes. The sweep angle varied between 10° and 45° for a range of Re between 800 and 2000 and subsequently maintained a constant sweep angle of approximately 46° for Re between 2000 and 7000. Similarly, the saddle point heights were at 4 mm for the lowest Re and reached a maximum of 7 mm at a Re of 2000 and higher.

SUPPLEMENTARY MATERIAL

See [supplementary material](#) for a video file corresponding to Figs. 5–11 (an animation of the series of snapshots shown in those figures), along with animated versions of Figs. 12 and 15.

ACKNOWLEDGMENTS

This work was supported by the U.S. Department of Energy (DOE) GATE Fellowship, the OSU Center for Automotive Research (CAR), and the Department of National Education (MEB) of Turkey.

- W. Li, T. Yao, H. Liu, and F. Wang, "Experimental investigation of flow regimes of axisymmetric and planar opposed jets," *AICHE J.* **57**, 1434–1445 (2011).
- V. Tesař, "Oscillator micromixer," *Chem. Eng. J.* **155**, 789–799 (2009).
- J. C. Rolon, D. Veynante, and J. P. Martin, "Counter jet stagnation flows," *Exp. Fluids* **11**, 313–324 (1991).
- R. P. Pawlowski, A. G. Salinger, J. N. Shadid, and T. J. Mountziaris, "Bifurcation and stability analysis of laminar isothermal counterflowing jets," *J. Fluid Mech.* **551**, 117–139 (2006).
- A. Nomoto, K. Yamamoto, and Y. Ohshio, "Axial impingement of two bounded jets," in *Proceedings of the 2nd International JSME Symposium on Fluid Machinery and Fluidics* (Tokyo, 1972), pp. 71–80.
- V. A. Denshchikov, V. N. Kondrat'ev, and A. N. Romashov, "Interaction between two opposed jets," *Fluid Dyn.* **13**, 924–926 (1978).
- V. A. Denshchikov, V. N. Kondrat'ev, A. N. Romashov, and V. M. Chubarov, "Auto-oscillations of planar impinging jets," *Fluid Dyn.* **18**, 460–462 (1983).
- W. Li, A. Sun, H. Liu, F. Wang, and Z. Yu, "Experimental and numerical study on stagnation point offset of turbulent opposed jets," *Chem. Eng. J.* **138**, 283–294 (2008).
- W.-F. Li, T.-L. Yao, and F.-C. Wang, "Study on factors influencing stagnation point offset of turbulent opposed jets," *AICHE J.* **56**, 2513–2522 (2010).
- W. Li, G. Huang, G. Tu, H. Liu, and F. Wang, "Experimental study of planar opposed jets with acoustic excitation," *Phys. Fluids* **25**(1), 014108 (2013).
- G. Stan and D. A. Johnson, "Experimental and numerical analysis of turbulent opposed impinging jets," *AIAA J.* **39**, 1901–1908 (2001).
- D. A. Johnson and P. E. Wood, "Self-sustained oscillations in opposed impinging jets in an enclosure," *Can. J. Chem. Eng.* **78**, 867–875 (2000).

- ¹³P. E. Dimotakis and G. L. Brown, "The mixing layer at high Reynolds number: Large-structure dynamics and entrainment," *J. Fluid Mech.* **78**, 535–560 (1976).
- ¹⁴D. Rockwell and E. Naudascher, "Self-sustained oscillations of impinging free shear layers," *Annu. Rev. Fluid Mech.* **11**, 67–94 (1979).
- ¹⁵C. M. Ho and N. S. Nosseir, "Dynamics of an impinging jet. Part 1. The feedback phenomenon," *J. Fluid Mech.* **105**, 119–142 (1981).
- ¹⁶D. Rockwell and E. Naudascher, "Review—Self-sustaining oscillations of flow past cavities," *J. Fluids Eng.* **100**, 152–165 (1978).
- ¹⁷J. R. Cho, "Numerical observations of a bifurcating plane impinging jet in a confined channel," *J. Visualization* **9**, 361–362 (2006).
- ¹⁸M. Hassaballa and S. Ziada, "Self-excited oscillations of two opposing planar air jets," *Phys. Fluids* **27**(1), 014109 (2015).
- ¹⁹R. J. Santos, A. M. T. Teixeira, and J. C. B. Lopes, "Study of mixing and chemical reaction in RIM," *Chem. Eng. Sci.* **60**, 2381–2398 (2005).
- ²⁰R. J. Santos, A. M. T. Teixeira, E. Ertugrul, M. A. Sultan, A. M. Karpinska, M. M. Dias, and J. C. B. Lopes, "Validation of a 2D CFD model for hydrodynamics studies in CIJ mixers," *Int. J. Chem. React. Eng.* **8**(1) (2010).
- ²¹M. A. Sultan, C. P. Fonte, M. M. Dias, J. C. B. Lopes, and R. J. Santos, "Experimental study of flow regime and mixing in T-jets mixers," *Chem. Eng. Sci.* **73**, 388–399 (2012).
- ²²D. A. Johnson, "Experimental and numerical examination of confined laminar opposed jets. Part I: Momentum balancing," *Int. Commun. Heat Mass Transfer* **27**, 443–454 (2000).
- ²³D. A. Johnson, "Experimental and numerical examination of confined laminar opposed jets. Part II: Momentum imbalance," *Int. Commun. Heat Mass Transfer* **27**, 455–463 (2000).
- ²⁴J. W. Gregory and M. N. Tomac, "A review of fluidic oscillator development and application for flow control," AIAA Paper 2013-2474, 2013.
- ²⁵S. Raghu, "Feedback-free fluidic oscillator and method," U.S. patent 6,253,782 (3 July 2001).
- ²⁶J. W. Gregory, J. P. Sullivan, and S. Raghu, "Visualization of jet mixing in a fluidic oscillator," *J. Visualization* **8**, 169–176 (2005).
- ²⁷J. W. Gregory, J. P. Sullivan, G. Raman, and S. Raghu, "Characterization of the microfluidic oscillator," *AIAA J.* **45**, 568–576 (2007).
- ²⁸M. N. Tomac and J. W. Gregory, "Frequency studies and scaling effects of jet interaction in a feedback-free fluidic oscillator," AIAA Paper 2012-1248, 2012.
- ²⁹G. Tu, W. Li, K. Du, G. Huang, and F. Wang, "Onset and influencing factors of deflecting oscillation in planar opposed jets," *Chem. Eng. J.* **247**, 125–133 (2014).
- ³⁰M. N. Tomac and J. W. Gregory, "Internal jet interaction in a fluidic oscillator at low flow rate," *Exp. Fluids* **55**(5), 1730 (2014).
- ³¹M. N. Tomac and J. W. Gregory, "Internal flow physics of a fluidic oscillator spray in the transition regime," *Atomization Sprays* **26**, 673–686 (2016).
- ³²A. Vernet, G. A. Kopp, J. A. Ferré, and F. Giralte, "Three-dimensional structure and momentum transfer in a turbulent cylinder wake," *J. Fluid Mech.* **394**, 303–337 (1999).